JOURNAL OF THEORETICAL AND APPLIED MECHANICS
49, 4, pp. 1115-1133, Warsaw 2011

A NEW FINITE ELEMENT TECHNIQUE FOR A PHASE FIELD MODEL OF BRITTLE FRACTURE

Charlotte Kuhn
Ralf Müller

University of Kaiserslautern, Institute of Applied Mechanics, Kaiserslautern, Germany
e-mail: chakuhn@rhrk.uni-kl.de; ram@rhrk.uni-kl.de

Phase field models for fracture employ a continuous field variable to indicate cracks. The width of the transition zone between cracked and uncracked areas is controlled by a regularization parameter. The numerical implementation of such models is sensible to the choice of this parameter in conjunction with the mesh size, as the mesh has to be fine enough to resolve high gradients of the crack field appearing in the transition zones. This is the main computational limit and challenge of the implementation. To overcome this limitation, a finite element method using exponential shape functions is introduced. Numerical examples show that these new shape functions perform better than standard Lagrange shape functions.

Key words: phase field, fracture, finite elements, exponential shape functions

1. Introduction

In phase field models for fracture, such as introduced by e.g. Aranson *et al.* (2000), Karma *et al.* (2001), Eastgate *et al.* (2002), Brener and Spatschek (2003) and Spatschek *et al.* (2006), cracks are represented by an additional field variable which is 0 if the material is cracked and 1 if it is undamaged, and cracking is addressed as a phase transition problem. All these phase field fracture models differ in detail, but commonly they feature a regularization parameter which has the dimension of length and controls the width of the transition zone where the crack field interpolates between 1 and 0. Finite element discretizations of those models are faced with the difficulty that the mesh has to be sufficiently fine in relation to the regularization length, as it has to be fine enough to resolve high gradients of the crack field appearing

around the cracks. On the other hand, the regularization parameter must be chosen sufficiently small in order to obtain reasonable results. Amor *et al.* (2009) suggest 1% of the global geometric dimension of the sample to be an appropriate value for the regularization parameter.

There are different approaches to meet the requirements for a sufficiently fine resolution on the one hand and to keep the computation time within bounds on the other hand. Eastgate *et al.* (2002) use Fourier transforms to solve the linear terms of their phase field model in order to increase the efficiency of the computations. However, this restricts the simulations to problems with periodic boundary conditions. A more common approach are adaptive remeshing strategies as can be found in Provatas *et al.* (1998) for a phase field solidification problem or in Bourdin and Chambolle (2000) for an approximation of the Mumford-Shah functional. Exploiting the fact that the phase field order parameter varies significantly only near an interface, the mesh is refined only where it is needed. This also applies for the material force based h-type mesh refinement algorithm suggested by Welschinger *et al.* (2010).

In the present work, we follow a different approach inspired by LaZghab *et al.* (2002). Special shape functions that qualitatively capture the shape of the crack field are constructed and implemented into the finite element code FEAP. These shape functions allow a coarser discretization without compromise on the accuracy of the results.

2. Material model

2.1. Governing equations

The core of the present phase field model of fracture is a regularized version of the variational formulation of brittle fracture by Francfort and Marigo (1998), which was introduced in Bourdin (2007). In the regularized model, the energy density of a broken linear elastic material with the stiffness tensor $\mathbf{C}$ and the cracking resistance $\mathcal{G}_c$ is approximated by

$$\begin{aligned}\psi(\boldsymbol{\varepsilon}, s) &= \psi^{el}(\boldsymbol{\varepsilon}, s) + \psi^{surf}(s) \\ &= \frac{1}{2}(s^2 + \eta)\boldsymbol{\varepsilon} \cdot (\mathbf{C}\boldsymbol{\varepsilon}) + \mathcal{G}_c\Big(\frac{1}{4\epsilon}(1-s)^2 + \epsilon|\nabla s|^2\Big)\end{aligned} \tag{2.1}$$

This regularized energy density ψ is a function of the linearized strain tensor $\boldsymbol{\varepsilon} = \frac{1}{2}(\nabla \boldsymbol{u} + (\nabla \boldsymbol{u})^\top)$, i.e. the symmetric part of the gradient of the displacements $\boldsymbol{u}$ and the continuous scalar field s, which describes the condition

of the material. Cracks are indicated by $s = 0$, while $s = 1$ is assigned to sound material. The parameter ϵ, appearing twice in the surface part ψ^{surf}, has the dimension of length and regulates the width of the transition zone between broken and unbroken material, where s interpolates between 0 and 1. The factor $(s^2 + \eta)$ in the elastic part of the energy density ψ^{el} accounts for the change in stiffness between broken and unbroken material. Consequently, material law (2.2) for the Cauchy stress tensor $\boldsymbol{\sigma}$ is modified to

$$\boldsymbol{\sigma} = \frac{\partial \psi}{\partial \boldsymbol{\varepsilon}} = (s^2 + \eta)\mathbf{C}\boldsymbol{\varepsilon} \tag{2.2}$$

Thus, the parameter $\eta \ll 1$ can be seen as the remaining stiffness if $s = 0$ and is needed to secure positive definiteness of the elastic energy. The local balance law for the Cauchy stress tensor

$$\operatorname{div} \boldsymbol{\sigma} = \mathbf{0} \tag{2.3}$$

where body forces and inertia terms are neglected, remains unaltered upon the regularization.

Interpreting s as the order parameter of a phase field model, $\dot{s}$ is assumed to be proportional to the variational derivative of the energy density ψ with respect to s, i.e.

$$\dot{s} = -M \frac{\delta \psi}{\delta s} = -M \Big[s\boldsymbol{\varepsilon} \cdot (\mathbf{C}\boldsymbol{\varepsilon}) - \mathcal{G}_c \Big(2\epsilon \Delta s + \frac{1 - s}{2\epsilon} \Big) \Big] \tag{2.4}$$

The mobility factor M is a constant, which describes the kinetics of the process. For sufficiently large values of M, the solution of the evolution equation can be considered as stationary. In order to take into consideration the irreversible character of cracking, $s(\boldsymbol{x}, t)$ is fixed to 0 for all future times $t > t^*$ if it becomes 0 at any time t^*.

2.2. 1D solution

The study of evolution equation (2.4) in one dimension is a very simple yet instructive way to understand the impact of the regularization parameter ϵ on the solution. Neglecting the elastic contribution and assuming the solution to be stationary $(\dot{s} = 0)$, the one dimensional evolution equation reduces to

$$s'' - \frac{s}{4\epsilon^2} = -\frac{1}{4\epsilon^2} \tag{2.5}$$

If boundary conditions $s(0) = 0$ and $s'(\pm L) = 0$ apply, Eq. (2.5) yields the (piecewise defined) solution

$$s(x) = 1 - \frac{\cosh\left(\frac{L-|x|}{2\epsilon}\right)}{\cosh\left(\frac{L}{2\epsilon}\right)} \tag{2.6}$$

which converges to

$$s(x) = 1 - \exp\left(-\frac{|x|}{2\epsilon}\right) \tag{2.7}$$

for $L \gg \epsilon$. Figure 1 shows plots of this function for different values of ϵ. The smaller ϵ gets, the higher gradients and curvatures of the solution $s(x)$ appear in the vicinity of the crack at $x = 0$. The limit $\epsilon \to 0$ yields a discontinuous function, which is 0 at $x = 0$ and 1 elsewhere.

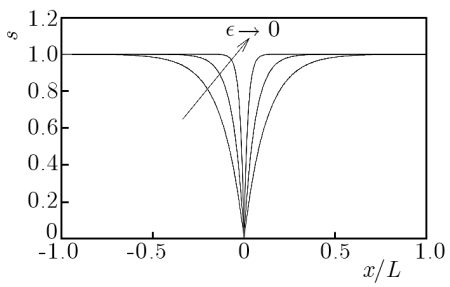

Fig. 1. 1D stationary crack field

3. Numerical implementation

3.1. Finite element formulation

The set of equations formed by balance equation (2.3) and evolution equation (2.4) together with the respective boundary conditions is solved using the finite element method. For the 2D case, 4 node quadrilateral elements with 3 degrees of freedom (u_x, u_y, s) per node are used in the discretization. The starting point of the FE formulation is the weak form of the field equations. With virtual displacements $\delta\boldsymbol{u}$ and δs, they read

$$\int_{\Omega} \nabla\delta\boldsymbol{u} \cdot \boldsymbol{\sigma}\, dV = \int_{\partial\Omega_t} \delta\boldsymbol{u} \cdot \boldsymbol{t}_n^*\, dA \tag{3.1}$$

and

$$\int_{\Omega} \Big[\delta s \frac{\dot{s}}{M} - \nabla \delta s \cdot \boldsymbol{q} + \delta s \Big(s\boldsymbol{\varepsilon} \cdot (\mathbf{C}\boldsymbol{\varepsilon}) + \frac{\mathcal{G}_c}{2\epsilon}(s-1)\Big)\Big]\, dV = \int_{\partial\Omega_q} \delta s q_n^*\, dA \tag{3.2}$$

with $\boldsymbol{q} = -2\mathcal{G}_c \epsilon \nabla s$. The boundary conditions for the stresses $\boldsymbol{\sigma}$ and for $\boldsymbol{q}$ are prescribed by the traction $\boldsymbol{t}_n^*$ and the normal flux q_n^*, which is usually assumed to be zero.

In the discretization, the displacements $\boldsymbol{u}$, the crack field s, as well as their virtual counterparts $\delta\boldsymbol{u}$ and δs are approximated by shape functions N_I^u, N_I^s, $N_I^{\delta u}$, and $N_I^{\delta s}$, which interpolate the respective nodal values $\hat{\boldsymbol{u}}_I$, $\hat{s}_I$, $\delta\hat{\boldsymbol{u}}_I$, and $\delta\hat{s}_I$. Using Voigt-notation – denoted by an underbar in the following – the approximations read

$$\begin{aligned} \underline{\boldsymbol{u}} &= \sum_{I=1}^{N} N_I^u \underline{\hat{\boldsymbol{u}}}_I & s &= \sum_{I=1}^{N} N_I^s \hat{s}_I \\ \underline{\delta\boldsymbol{u}} &= \sum_{I=1}^{N} N_I^{\delta u} \underline{\delta\hat{\boldsymbol{u}}}_I & \delta s &= \sum_{I=1}^{N} N_I^{\delta s} \delta\hat{s}_I \end{aligned} \tag{3.3}$$

With the matrices

$$\begin{aligned} [\underline{B}_I^u] &= \begin{bmatrix} N_{I,x}^u & 0 \\ 0 & N_{I,y}^u \\ N_{I,y}^u & N_{I,x}^u \end{bmatrix} & [\underline{B}_I^s] &= \begin{bmatrix} N_{I,x}^s \\ N_{I,y}^s \end{bmatrix} \\ [\underline{B}_I^{\delta u}] &= \begin{bmatrix} N_{I,x}^{\delta u} & 0 \\ 0 & N_{I,y}^{\delta u} \\ N_{I,y}^{\delta u} & N_{I,x}^{\delta u} \end{bmatrix} & [\underline{B}_I^{\delta s}] &= \begin{bmatrix} N_{I,x}^{\delta s} \\ N_{I,y}^{\delta s} \end{bmatrix} \end{aligned} \tag{3.4}$$

defined by the derivatives of the shape functions, the approximations of the gradient expressions yield

$$\begin{aligned} \underline{\boldsymbol{\varepsilon}} &= \sum_{I=1}^{N} [\underline{B}_I^u] \underline{\hat{\boldsymbol{u}}}_I & \underline{\nabla s} &= \sum_{I=1}^{N} [\underline{B}_I^s] \hat{s}_I \\ \underline{\delta\boldsymbol{\varepsilon}} &= \sum_{I=1}^{N} [\underline{B}_I^{\delta u}] \underline{\delta\hat{\boldsymbol{u}}}_I & \underline{\nabla \delta s} &= \textstyle\sum_{I=1}^{N} [\underline{B}_I^{\delta s}] \delta\hat{s}_I \end{aligned} \tag{3.5}$$

As Eq. (3.1) and Eq. (3.2) must hold for any choice of the virtual quantities $\delta\boldsymbol{u}$ and δs, the respective nodal values cancel out of the system of equations. Thus, the left hand sides of Eq. (3.1) and Eq. (3.2) form the nodal residuals

$$[\underline{R}_I] = \begin{bmatrix} \underline{R}_I^u \\ R_I^s \end{bmatrix} = \int\limits_\Omega \begin{bmatrix} [\underline{B}_I^{\delta u}]^\top \underline{\boldsymbol{\sigma}} \\ N_I^{\delta s} \dfrac{\dot{s}}{M} - [\underline{B}_I^{\delta s}]^\top \underline{\boldsymbol{q}} + N_I^{\delta s} \Big(s \underline{\boldsymbol{\varepsilon}}^\top \cdot [\underline{\mathbf{C}} \underline{\boldsymbol{\varepsilon}}] + \dfrac{\mathcal{G}_c}{2\epsilon}(s-1) \Big) \end{bmatrix} dV \tag{3.6}$$

The time integration of the transient terms is performed with the implicit Euler method, and the overall nonlinear set of equations is solved iteratively with a Newton-Raphson algorithm. For this algorithm, the stiffness matrix $[K_{IJ}]$ and the damping matrix $[D_{IJ}]$ must be provided. They are obtained by derivation of the nodal residuals $[\underline{R}_I]$ with respect to the nodal values $(\hat{\boldsymbol{u}}_J, \hat{s}_J)$

$$[\underline{K}_{IJ}] = \int\limits_\Omega \begin{bmatrix} [\underline{B}_I^{\delta u}]^\top (s^2 + \eta) \underline{\mathbf{C}} [\underline{B}_J^u] & [\underline{B}_I^{\delta u}]^\top 2s \underline{\mathbf{C}} \underline{\boldsymbol{\varepsilon}} N_J^s \\ N_I^{\delta s} 2s (\underline{\mathbf{C}} \underline{\boldsymbol{\varepsilon}})^\top [\underline{B}_J^u] & 2\mathcal{G}_c \epsilon [\underline{B}_I^{\delta s}]^\top [\underline{B}_J^s] + N_I^{\delta s} \Big(\underline{\boldsymbol{\varepsilon}}^\top \cdot \underline{\mathbf{C}} \underline{\boldsymbol{\varepsilon}} + \dfrac{\mathcal{G}_c}{2\epsilon} \Big) N_J^s \end{bmatrix} dV \tag{3.7}$$

$$\underline{D}_{IJ} = \int\limits_\Omega \begin{bmatrix} 0 & 0 \\ 0 & \dfrac{1}{M} N_I^{\delta s} N_J^s \end{bmatrix} dV$$

If the same shape functions are chosen for the approximation of the actual values and the virtual quantities, i.e. $N_I^u = N_I^{\delta u}$ and $N_I^s = N_I^{\delta s}$, the assembled system matrix becomes symmetric; differently chosen shape functions render a non-symmetric system matrix.

4. Exponential shape functions

Usually, the linear Lagrangian shape functions

$$N_I^l(\xi, \eta) = \frac{1}{4}(1 + \xi_I \xi)(1 + \eta_I \eta) \qquad I = 1, \ldots, 4 \tag{4.1}$$

with (ξ_I, η_I) according to Fig. 2 are used for all the shape functions N_I^u, $N_I^{\delta u}$, N_I^s, and $N_I^{\delta s}$ as well as for the approximation of the geometry within the isoparametric concept

$$\boldsymbol{x} = \sum_{I=1}^{N} N_I^l \hat{\boldsymbol{x}}_I \tag{4.2}$$

The computational limit of this method becomes apparent looking at the 3D representation of the phase field of an initial crack in an unloaded sample in Fig. 3. The mesh has to be chosen fine enough to resolve the high gradients and curvatures of the phase field in the transition zone between cracked and uncracked areas. In this example, the regularization parameter ϵ was set

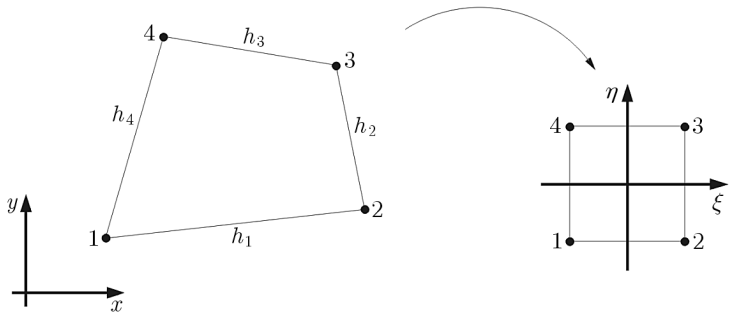

Fig. 2. Node and edge numbering of the quadrilateral element in global (left) and natural coordinates (right)

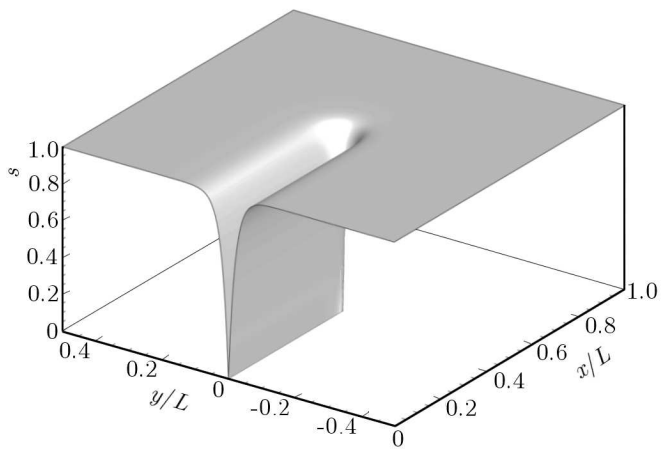

Fig. 3. 3D representation of the phase field of a crack

to $0.01L$, where L is the edge length of the square sample. A uniform mesh with 200×200 elements was used for the discretization, thus the edge length of the elements is $h = 0.005L$. Bourdin *et al.* (2008) show that linear triangular elements overestimate the surface energy by a factor $f(h/\epsilon) = 1 + h/4\epsilon$, and hence different authors (Amor *et al.*, 2009; Miehe *et al.*, 2010) empirically found $h \approx \epsilon$ as an upper bound for the element size in a 2D setting.

Figure 4 compares the computed phase field values to analytical solution (2.7) at the specimen edge far behind the crack tip along the segment $\{0\} \times [0, 0.5L]$ and in front of the crack tip along the segment $[0.5L, 1L] \times \{0\}$ for two different values of ϵ. At the specimen edge, the analytical solution captures the computed values quite perfectly, yet in front of the crack tip the computed crack field is even steeper than the analytical solution predicts. However, the shape still resembles an exponential function, and the impact of ϵ remains the same, i.e. the smaller ϵ, the smaller the transition zone between

$s = 0$ and $s = 1$. Hence, particularly along the crack lips but also at the crack tip, the shape functions derived from the 1D solution promise a very accurate interpolation of the crack field.

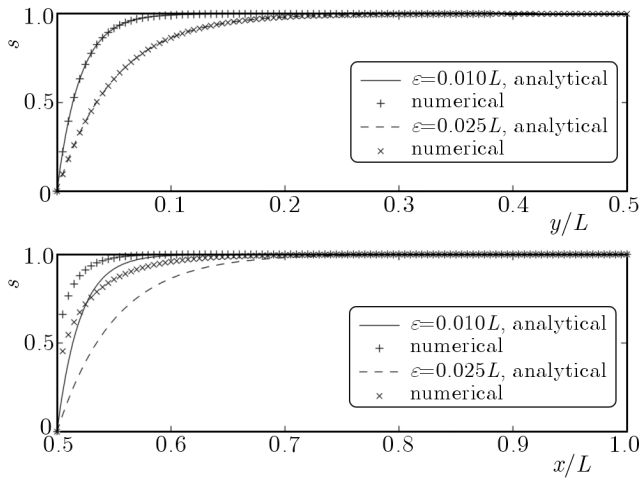

Fig. 4. Comparison of the computed 2D phase field to 1D solution (2.7) at the specimen edge (top) and at the crack tip (bottom)

4.1. Construction of 1D exponential shape functions

The simulation of extrusion processes, where shear boundary layers characterized by an exponential velocity profile need to be resolved, is faced with a similar problem. As an alternative to a fine numerical resolution, LaZghab *et al.* (2002) introduce exponential shape functions that capture the shape of the sharp velocity field. Since the numerical 2D solution shows the same characteristic exponential shape that was found for the 1D case, this ansatz seems also very promising for the discretization of the present phase field model. Adapted to the present phase field model, these 1D shape functions read

$$\begin{aligned} \bar{N}_1^e(\xi,\delta) &= 1 - \frac{\exp\left(-\frac{\delta(1+\xi)}{4}\right) - 1}{\exp\left(-\frac{\delta}{2}\right) - 1} \\ \bar{N}_2^e(\xi,\delta) &= \frac{\exp\left(-\frac{\delta(1+\xi)}{4}\right) - 1}{\exp\left(-\frac{\delta}{2}\right) - 1} \end{aligned} \tag{4.3}$$

in natural coordinates on the interval $[-1, 1]$. The coefficient $\delta = h/\epsilon$ in the exponential shape functions is the ratio of the element size h and the

regularization parameter ϵ. In the limit case $\delta \to 0$ or equivalently $h \to 0$ these shape functions converge to the one dimensional linear shape functions, i.e.

$$\lim_{\delta\to 0} \bar{N}_1^e(\xi,\delta) = \frac{1-\xi}{2} = N_1^l(\xi) \qquad \lim_{\delta\to 0} \bar{N}_2^e(\xi,\delta) = \frac{1+\xi}{2} = N_2^l(\xi) \tag{4.4}$$

These shape functions are designed to perfectly match analytical solution (2.7), if $\hat{s}_1 \leqslant \hat{s}_2$ holds for the according nodal values. However, they do not match in the other case, see Fig. 5. This problem arises due to the fact that the exponential shape functions are unsymmetric with respect to ξ, i.e. $\bar{N}_1^e(-\xi) \neq \bar{N}_2^e(\xi)$. In order to resolve this deficiency, the orientation of the exponential shape functions needs to be switched according to the nodal values of s

$$\begin{aligned} N_1^e(\xi) &= \begin{cases} \bar{N}_1^e(\xi,\delta) & \text{if } \hat{s}_1 \leqslant \hat{s}_2 \\ \bar{N}_2^e(-\xi,\delta) & \text{if } \hat{s}_1 > \hat{s}_2 \end{cases} \\ N_2^e(\xi) &= \begin{cases} \bar{N}_2^e(\xi,\delta) & \text{if } \hat{s}_1 \leqslant \hat{s}_2 \\ \bar{N}_1^e(-\xi,\delta) & \text{if } \hat{s}_1 > \hat{s}_2 \end{cases} \end{aligned} \tag{4.5}$$

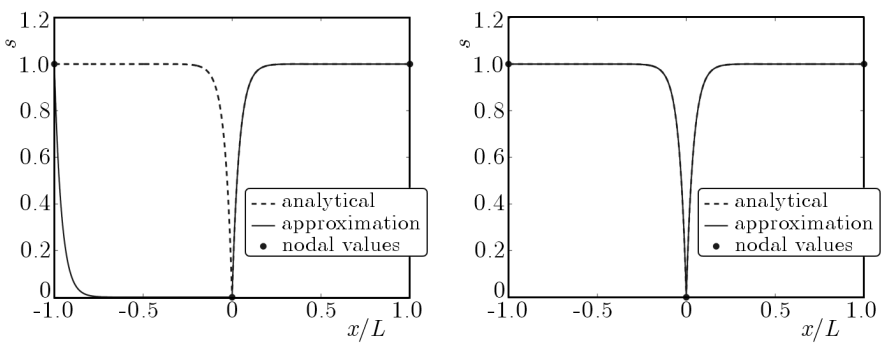

Fig. 5. Approximation with unswitched shape functions (left), and switched shape functions (right)

The respective derivatives which are necessary for the approximation of the gradient ∇s in the finite element discretization are

$$\frac{\partial N_1^e}{\partial \xi} = \frac{\delta}{4} \frac{\exp\left(-\frac{\delta(1\pm\xi)}{4}\right)}{\exp\left(-\frac{\delta}{2}\right) - 1} \qquad \frac{\partial N_2^e}{\partial \xi} = -\frac{\delta}{4} \frac{\exp\left(-\frac{\delta(1\pm\xi)}{4}\right)}{\exp\left(-\frac{\delta}{2}\right) - 1} \tag{4.6}$$

where $+$ applies for $\hat{s}_1 \leqslant \hat{s}_2$ and $-$ for $\hat{s}_1 > \hat{s}_2$.

4.2. Extension to 2D

The velocity field for which the exponential shape functions were constructed by LaZghab *et al.* (2002) is exponential only in one direction. Thus, it is sufficient to combine the 1D exponential shape functions with linear 1D shape functions in the second direction in order to obtain shape functions for a 2D quadrilateral element. In our case, this would be sufficient for the discretization of the crack lips but not at the crack tip. Therefore we use the 1D exponential shape functions in both directions to construct 2D shape functions.

The 2D linear shape function of each single element node can be obtained by multiplying the 1D linear shape functions belonging to the adjacent edges of the respective node. The adaptation of this strategy for the construction of 2D exponential shape functions yields

$$\begin{aligned} \bar{N}_1^e(\xi,\eta,\delta_i) &= N_1^e(\xi,\delta_1)N_1^e(\eta,\delta_4) & \bar{N}_2^e(\xi,\eta,\delta_i) &= N_2^e(\xi,\delta_1)N_1^e(\eta,\delta_2) \\ \bar{N}_3^e(\xi,\eta,\delta_i) &= N_2^e(\xi,\delta_3)N_2^e(\eta,\delta_2) & \bar{N}_4^e(\xi,\eta,\delta_i) &= N_1^e(\xi,\delta_3)N_2^e(\eta,\delta_4) \end{aligned} \tag{4.7}$$

where the element nodes and the element edges are numbered according to Fig. 2. Each shape function depends on the ratio $\delta_i = h_i/\epsilon$ of both adjacent element edges. For an appropriate approximation behavior, it is postulated that the orientation of the 1D shape functions of opposite edges must be the same. The so constructed shape functions possess the Kronecker delta property, i.e. $\bar{N}_I^e(\xi_J,\eta_J,\delta_i) = \delta_{IJ}$. Continuity across element borders holds, if the orientation of the shared edge of two neighbor elements is the same. However, summation of the 4 shape functions gives

$$\sum_{I=1}^{4} \bar{N}_I^e(\xi,\eta,\delta_i) = 1 - \underbrace{[N_1^e(\xi,\delta_1) - N_1^e(\xi,\delta_3)][N_1^e(\eta,\delta_2) - N_1^e(\eta,\delta_4)]}_{=R(\xi,\eta,\delta_i)} \tag{4.8}$$

Thus, partition of unity does not hold in every case. If arbitrary quadrilateral elements are used, the shape functions can be modified, for example, to

$$N_I^e(\xi,\eta,\delta_i) = \bar{N}_I^e(\xi,\eta,\delta_i) + \frac{1}{4}R(\xi,\eta,\delta_i) \qquad \text{for} \quad I = 1,\ldots,4. \tag{4.9}$$

Under the constraint that the orientation of the 1D shape functions of opposite edges must be the same, the correction term $R(\xi,\eta,\delta_i)$ vanishes whenever

$$\delta_1 = \delta_3 \qquad \text{or} \qquad \delta_2 = \delta_4 \tag{4.10}$$

holds. This is especially true for square and rectangular elements as used in Section 5.

As $R(\xi, \eta, \delta_i)$ vanishes on the entire boundary of the unit square $[-1,1] \times [-1,1]$, this correction does not disturb the continuity and the Kronecker delta property of the shape functions. Furthermore, one can show that $\lim_{\delta_i \to 0} R(\xi, \eta, \delta_i) = 0$.

4.3. Derivatives of the 2D exponential shape functions

The computation of the derivatives $N^e_{I,\xi}$ and $N^e_{I,\eta}$ of the exponential shape functions with respect to the natural coordinates ξ and η is straightforward, using the 1D derivatives in Eq. (4.6). The derivatives $N^e_{I,x}$ and $N^e_{I,y}$ with respect to the global coordinates x and y follow from the relation

$$\begin{aligned} \frac{\partial N^e_I}{\partial \xi} &= \frac{\partial N^e_I}{\partial x}\frac{\partial x}{\partial \xi} + \frac{\partial N^e_I}{\partial y}\frac{\partial y}{\partial \xi} \\ \frac{\partial N^e_I}{\partial \eta} &= \frac{\partial N^e_I}{\partial x}\frac{\partial x}{\partial \eta} + \frac{\partial N^e_I}{\partial y}\frac{\partial y}{\partial \eta} \end{aligned} \quad \Leftrightarrow \quad \begin{bmatrix} N^e_{I,\xi} \\ N^e_{I,\eta} \end{bmatrix} = \underbrace{\begin{bmatrix} x_{,\xi} & y_{,\xi} \\ x_{,\eta} & y_{,\eta} \end{bmatrix}}_{=\mathbf{J}} \begin{bmatrix} N^e_{I,x} \\ N^e_{I,y} \end{bmatrix} \tag{4.11}$$

where

$$\mathbf{J} = \sum_{I=1}^{4} \begin{bmatrix} N^l_{I,\xi}\hat{x}_I & N^l_{I,\xi}\hat{y}_I \\ N^l_{I,\eta}\hat{x}_I & N^l_{I,\eta}\hat{y}_I \end{bmatrix} \tag{4.12}$$

if the geometry is approximated with linear shape functions according to Eq. (4.2).

5. Results

The performance of the 2D exponential shape functions is tested in this section. In all simulations, linear shape functions (4.1) were used for the approximation of the geometry and the actual and virtual displacements, i.e. $N^u_I = N^{\delta u}_I = N^l_I$. Three different versions of approximating the crack field s and its virtual counterpart δs are compared to each other: The standard approximation with linear shape functions $N^s_I = N^{\delta s}_I = N^l_I$ (labeled lin/lin), the complete approximation with exponential shape functions $N^s_I = N^{\delta s}_I = N^e_I$ (labeled exp/exp), and a mixed formulation with $N^s_I = N^e_I$ but $N^{\delta s}_I = N^l_I$ (labeled lin/exp). As regular meshes with solely rectangular or square elements were used, condition (4.10) holds and the correction term R of the exponential shape function vanishes.

5.1. Stationary evolution equation

For the first numerical assessment of the 2D exponential shape functions, we stick to the example of Section 4.2. No mechanical loads are applied and the problem reduces to solving evolution equation (2.4) under the constraint $s(x,y) = 0$ if $(x,y) \in [0, L/2] \times \{0\}$. A regular mesh with square elements is used for the discretization. Figure 6 shows the crack field for $\epsilon = 0.01L$ computed with only 4×4 elements ($\delta_i = 25$) and 5 Gauss points per direction. With such a coarse mesh, the standard approach using linear shape functions fails to give a reasonable solution. However, both computations using the exponential shape functions yield already qualitatively very good results, which are at first sight almost identical. Only directly in front of the crack tip the result from the mixed formulation (lin/exp) is even a bit more accurate.

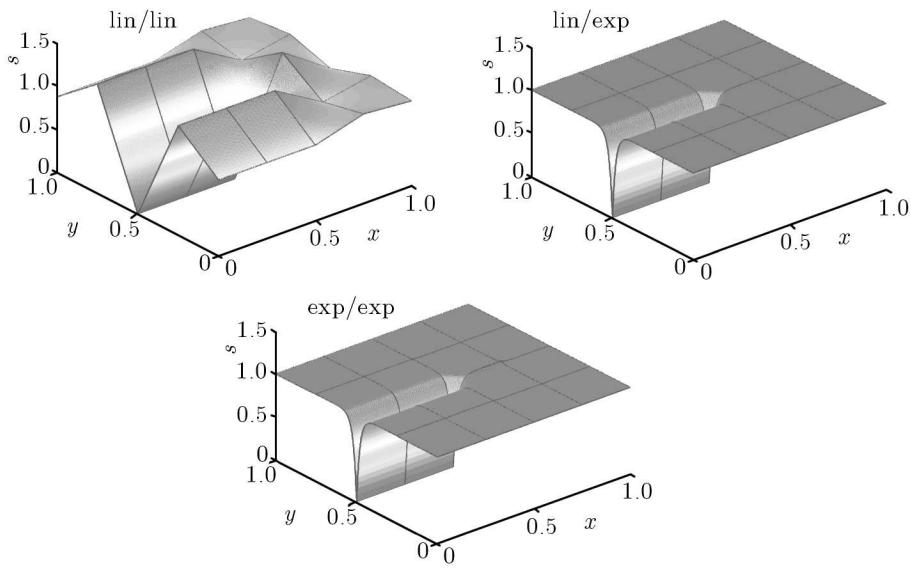

Fig. 6. Comparison of the crack field computed with 4×4 elements

Figure 7 shows the results from a further investigation of the performance of the exponential shape functions in this example. For $\epsilon = 0.01L$ (left) and $\epsilon = 0.002L$ (right), the stationary solution of the evolution equation was computed with meshes within the range of 2×2 to 400×400 elements. The surface energy

$$E^{surf} = \int_{\Omega} \psi^{surf}(s)\, dV = \int_{\Omega} \mathcal{G}_c \Big(\frac{1}{4\epsilon}(1-s)^2 + \epsilon |\nabla s|^2 \Big)\, dV \tag{5.1}$$

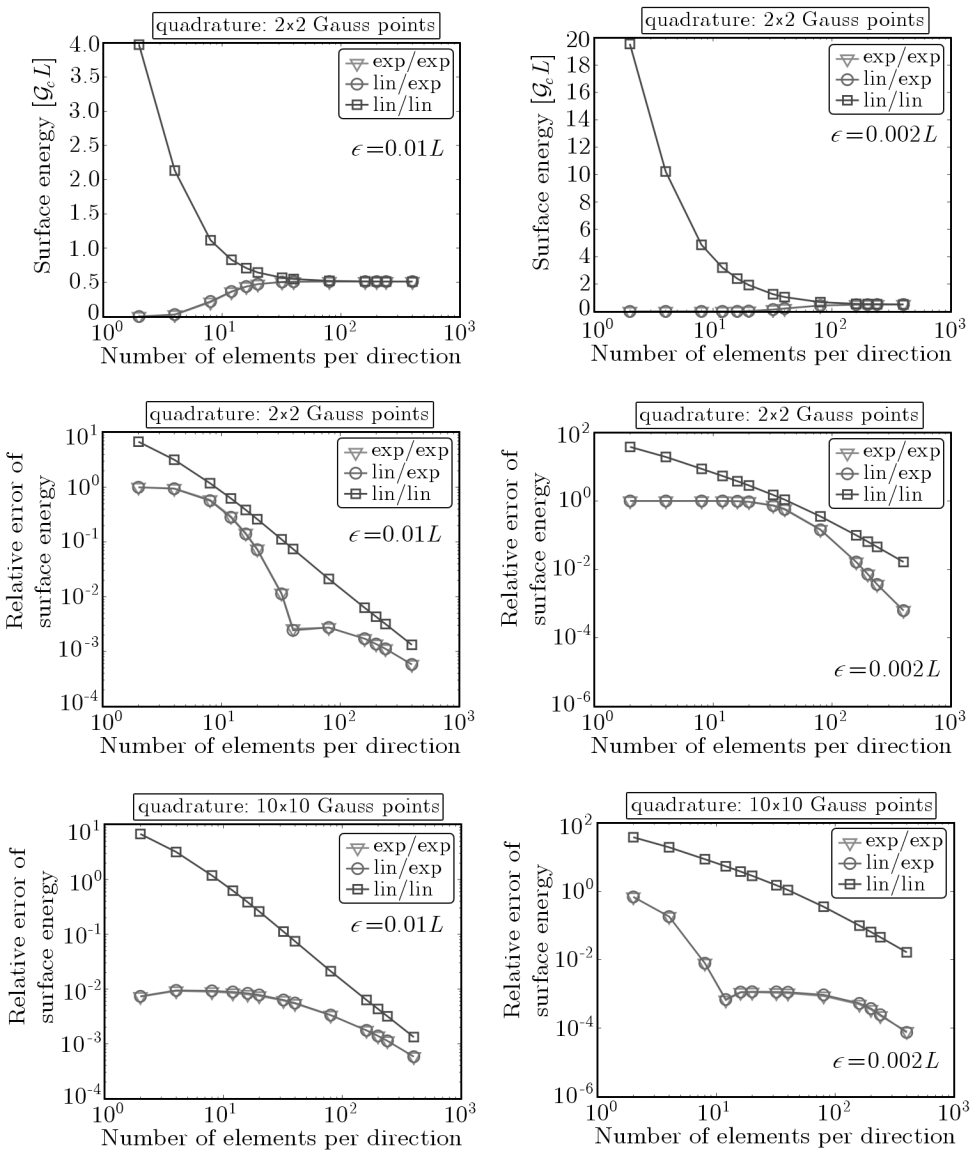

Fig. 7. Evaluation of the surface energy

associated with the computed crack field is plotted in the left column of Fig. 7. The results obtained with both versions using the exponential shape functions are very similar. Even if a very coarse mesh is used, the surface energy is only slightly underestimated, while the solution with linear shape functions overestimates it by far. This is even more significant for the smaller value of ϵ.

In standard 2D finite element analysis, the integrals in residuals (3.6), stiffness matrix $(3.7)_1$, and damping matrix $(3.7)_2$ are computed using the Gauss quadrature formula with 2 integration points per direction. This quadrature method was used for the computation of the surface energy in the first row and the relative error of the surface energy in the second row of Fig. 7. The usage of the exponential shape functions yields a smaller relative error, yet their full potential only reveals itself if a more precise quadrature method is employed. The plots in the last row of Fig. 7 show the relative error in the surface energy, if 10×10 Gauss points are used for the integration. Especially for large values of the ratio $\delta = h/\epsilon$, this measure drastically decreases the relative error compared to the calculations with 2×2 quadrature points. Thus, in the latter case, the largest part of the error is due to the quadrature method. Standard linear shape functions and a non-uniform mesh with square elements of edge length $h = 7.1429 \cdot 10^{-4} L$ and $h = 4.8828 \cdot 10^{-4} L$ in the vicinity the crack, were used to obtain the reference solutions $E^{surf} = 0.51017344300\, \mathcal{G}_c L$ for $\epsilon = 0.01L$ and $E^{surf} = 0.50241252899\, \mathcal{G}_c L$ for $\epsilon = 0.002L$, respectively.

5.2. Crack growth

In this section, we test the performance of the exponential shape functions, when mechanical loads are applied to the system, i.e. the whole set of coupled equations has to be solved. Therefore, the sample is now loaded by a linear increasing displacement load $\boldsymbol{u}^*(t) = \sqrt{\mathcal{G}_c L/(2\mu)}\, t$ along the edge $[0, L] \times \{0.5L\}$. With this scaling of the displacements, the geometric length L and the cracking resistance $\mathcal{G}_c$ can be factored out from the energy functional. If the mobility M is chosen large enough to assume quasistatic cracking, then the solution of the coupled problem only depends on the ratio of the Lamé constants λ/μ and the regularization parameter ϵ in conjunction with L. The simulations presented here, refer to the case of equal Lamé constants $\lambda = \mu$ with plane strain assumptions, corresponding to a Poisson's ratio of $\nu = 0.25$ and the regularization parameter $\epsilon = 0.0005L$. Exploiting the symmetry of the problem, only half of the area is discretized. The discretization in x-direction is done with 150 elements. A varying number of n elements plus one row of elements of fixed height, to model the initial crack, discretize the structure in the y-direction, see Fig. 8. The FEM solutions based on the exponential shape functions in Section 5.1 were very similar, no matter if linear or exponential shape functions were used for the discretization of δs. The mixed formulation yields an unsymmetric system matrix, which is computationally more expensive, and thus this option is not treated in the following. Gauss quadrature with 5×5 integration points was used for the integration.

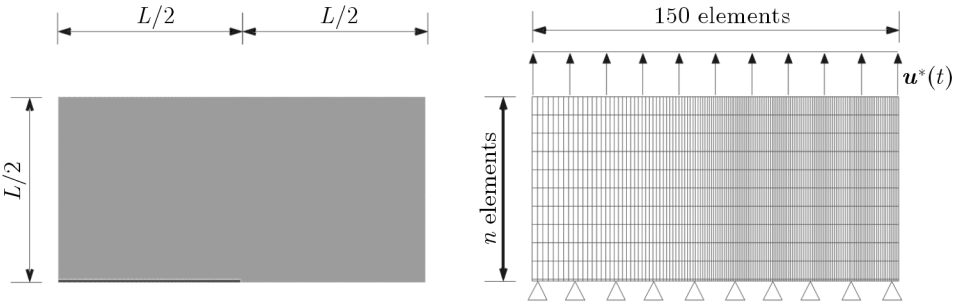

Fig. 8. Simulation setup: contour plot of the initial crack field (left) and finite element mesh (right)

The two plots in Fig. 9 show the evolution of the elastic energy with respect to the load factor t for different numbers of n. At the beginning, the elastic energy increases with the loading until rupture occurs and it drops to zero. Impressively, the simulation with only $n = 2$ elements in the y-direction already gives a qualitatively good result not that far away from the simulations with more elements, when the exponential shape functions are employed. Using the standard linear shape functions, no rupture can be observed in the simulation with $n = 2$ elements up to a load factor of $t = 3$, which is about twice the actual critical loading. Also the simulation with $n = 16$ elements still overestimates the critical loading by far. Only the simulations with more elements produce as accurate results as the simulations with the exponential shape functions. Seeking for a reliable prediction of the stability of a structure, another advantage of the exponential shape functions is that they underestimate the true critical load value. The overestimation of the critical load value of the linear shape functions stems from the overestimation of the surface energy associated with the initial crack.

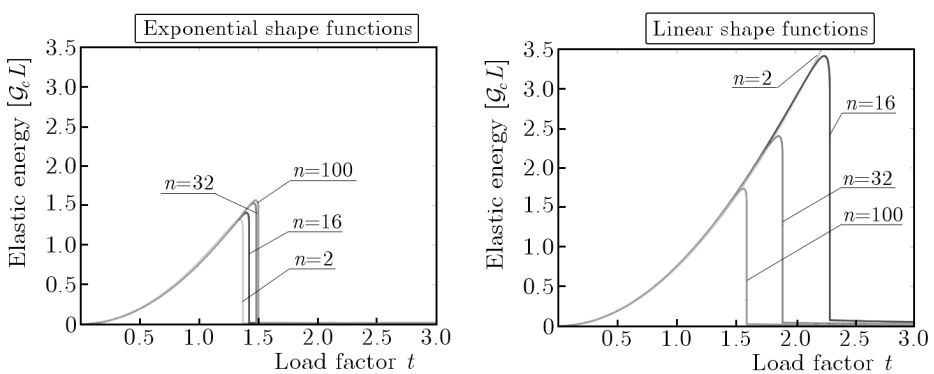

Fig. 9. Elastic energy

6. Conclusions and outlook

The aim of this work was to provide an alternative to an expensive mesh refinement in finite element simulations of a phase field model for fracture in cases where the regularization parameter is very small. To this end, special shape functions, which capture the analytical stationary solution of the 1D crack field, were derived and implemented into a 2D element of a finite element code. As the exponential terms of these shape functions are controlled by the regularization length of the phase field model, they are able to adjust to the shape of the crack field, which depends on this parameter in a similar way. This adaptive property of the exponential shape functions allows computations with virtually arbitrarily small values of the regularization parameter, which would require an extensive mesh refinement if standard linear shape functions are used.

The performance of the 2D exponential shape functions has been evaluated in two examples, the first considering only the stationary evolution equation, the second considering the whole coupled problem of the mechanical force balance and the evolution equation. In both cases, usage of the exponential shape functions allowed a considerable reduction of the level of refinement without compromise on the accuracy of the results.

Two different approaches of incorporating the exponential shape functions in the finite element scheme have been tested. The mixed formulation with exponential shape functions only for the crack field itself and linear shape functions for the test functions seems to yield slightly more accurate results than the purely exponential formulation. Yet the prize to pay is an unsymmetric system matrix causing a significant increase in the computation time and required memory. In this regard, the purely exponential formulation is to be preferred.

Another issue that comes up when the exponential shape functions are used is the choice of an appropriate quadrature method for computation of the integrals in the residual and the system matrix. The standard integration scheme using 2 Gauss quadrature points per direction fails to approximate the integrals sufficiently well if there are large gradients in the crack field, and the ratio $\delta = h/\epsilon$ of element length and regularization parameter becomes too large. In this case, a more exact quadrature method with more integration points has to be employed. Yet, this again increases the computation time. Thus, an automatic choice of a reasonable number of quadrature points in conjunction with δ is useful.

So far, the simulations with the elements with exponential shape functions are restricted to simple examples, where the crack path is known in advance. This is due to the fact that the adequate orientation of those elements with respect to the crack position has to be defined *a priori*. The considered phase field model, however, naturally contains the possibility to determine also complicated crack paths including crack initiations and crack branching. To this end, the development of a stable algorithm that, if necessary, redefines the orientation of the exponential elements after every time step is essential.

The exponential shape functions are especially adequate to approximate the crack field in fractured zones. In undamaged zones, where the crack field is almost constant, the linear shape functions do as well. Due to the exponential terms involved, the evaluation of the exponential shape functions is computationally more expensive than the evaluation of linear shape functions. Therefore, they should only be employed where they are needed, i.e. in the vicinity of cracks. A combination of both raises the problem of constructing blending elements which blend elements with exponential shape functions to those with linear shape functions. The difficulty here is to preserve continuity and partition of unity properties of the shape functions.

In this work, the focus was laid on improving the shape functions for the crack field. However, also the displacement field features high gradients around the cracks, which also cannot be captured by the linear shape functions if the mesh is too coarse. Thus, further room for improvement lies in enhancing the shape functions used for the approximation of the displacement field. An ansatz going in this direction would be the construction of a 9 node element, combining the exponential shape functions with 3 nodes per direction, which were also introduced in LaZghab *et al.* (2002), with quadratic Lagrange shape functions for the displacement field.

References

1. Amor H., Marigo J.-J., Maurini C., 2009, Regularized formulation of the variational brittle fracture with unilateral contact: Numerical experiments, *Journal of the Mechanics and Physics of Solids*, **57**, 8, 1209-1229

2. Aranson I.S, Kalatsky V.A., Vinokur V.M., 2000, Continuum field description of crack propagation, *Physical Review Letters*, **85**, 1, 118-121

3. Bourdin B., 2007, Numerical implementation of the variational formulation of quasi-static brittle fracture, *Interfaces and Free Boundaries*, **9**, 411-430

4. Bourdin B., Chambolle A., 2000, Implementation of an adaptive finite-element approximation of the mumford-shah functional, *Numerische Mathematik*, **85**, 4, 609-646

5. Bourdin B., Francfort G., Marigo J.-J., 2008, The variational approach to fracture, *Journal of Elasticity*, **91**, 1, 5-148

6. Brener E.A., Spatschek R., 2003, Fast crack propagation by surface diffusion, *Physical Review E*, **67**, 1, 016112

7. Eastgate L.O., Sethna J.P., Rauscher M., Cretegny T., Chen C.-S., Myers C.R., 2002, Fracture in mode I using a conserved phase-field model, *Physical Review E*, **65**, 3, 036117

8. Francfort G.A., Marigo J.-J., 1998, Revisiting brittle fracture as an energy minimization problem, *Journal of the Mechanics and Physics of Solids*, **46**, 8, 1319-1342

9. Karma A., Kessler D.A., Levine H., 2001, Phase-field model of mode iii dynamic fracture, *Physical Review Letters*, **87**, 4, 45501

10. LaZghab S., Aukrust T., Holthe K., 2002, Adaptive exponential finite elements for the shear boundary layer in the bearing channel during extrusion, *Computer Methods in Applied Mechanics and Engineering*, **191**, 11/12, 1113-1128

11. Miehe C., Welschinger F., Hofacker M., 2010, Thermodynamically consistent phase-field models for fracture: Variational principles and multi-field fe implementations, *International Journal for Numerical Methods in Engineering*, **83**, 10, 1273-1311

12. Provatas N., Goldenfeld N., Dantzig J., 1998, Efficient computation of dendritic microstructures using adaptive mesh refinement, *Physical Review Letters*, **80**, 15, 3308-3311

13. Spatschek R., Hartmann M., Brener E., Müller-Krumbhaar H., Kassner K., 2006, Phase field modeling of fast crack propagation, *Physical Review Letters*, **96**, 1, 015502

14. Welschinger F., Hofacker M., Miehe C., 2010, Configurational-force-based adaptive fe solver for a phase field model of fracture, [In:] *Proceedings in Applied Mathematics and Mechanics*, **10**, 689-692

Nowa metoda elementów skończonych dla modelu pól fazowych przy opisie kruchego pękania

Streszczenie

Modele pól fazowych w opisie procesu pękania wykorzystują zmienne ciągłe pola do wykrywania pęknięć. Szerokość strefy przejściowej pomiędzy obszarem pęknięcia a nieuszkodzonym jest opisana parametrem regularyzacji. Numeryczna implementacja takich modeli jest wrażliwa na dobór tego parametru w połączeniu z rozmiarem siatki elementów skończonych, która musi być odpowiednio gęsta, by uwzględnić duże gradienty pola z pęknięciem w strefie przejściowej. Jest to główne ograniczenie w przeprowadzaniu obliczeń i duże wyzwanie symulacyjne. W pracy zaproponowano użycie wykładniczych funkcji kształtu do metody elementów skończonych w celu eliminacji tego ograniczenia. Przedstawione przykłady pokazały, że zastosowanie funkcji wykładniczych zamiast standardowych funkcji Lagrange'a wyraźnie poprawiło wydajność numeryczną modeli.

Manuscript received December 1, 2010; accepted for print January 31, 2011